Geophysical Research Letters

RESEARCH LETTER
10.1029/2018GL078434

Key Points:
- Differential stress induces both anisotropy and damage
- Anisotropy is stress rather than damage sensitive
- Unloading leads to recovery of both damage and elastic anisotropy inferred from elastic velocity measurements

Supporting Information:
- Supporting Information S1
- Data Set S1
- Data Set S2
- Data Set S3
- Data Set S4
- Data Set S5

Correspondence to:
F. X. Passelègue,
passelegue@gmail.com

Citation:
Passelègue F. X., Pimienta, L., Faulkner, D. R., Schubnel, A., Fortin, J. N., & Guéguen, Y. (2018). Development and recovery of stress-induced elastic anisotropy during cyclic loading experiment on Westerly granite. *Geophysical Research Letters*, *45*, 8156–8166. https://doi.org/10.1029/2018GL078434

Received 28 APR 2018
Accepted 20 JUL 2018
Accepted article online 25 JUL 2018
Published online 17 AUG 2018

Development and Recovery of Stress-Induced Elastic Anisotropy During Cyclic Loading Experiment on Westerly Granite

François. X. Passelègue[1,2,3], Lucas Pimienta[2,3], Daniel Faulkner[4], Alexandre Schubnel[2], Jérôme Fortin[2], and Yves Guéguen[2]

[1]SEAES, The University of Manchester, Manchester, UK, [2]Laboratoire de Géologie, CNRS UMR, École Normale Supérieure, Paris, France, [3]Civil Engineering, EPFL Lausanne, Lausanne, Switzerland, [4]School of Environmental, The University of Liverpool, Liverpool, UK

Abstract In the upper crust, where brittle deformation mechanisms dominate, the development of crack networks subject to anisotropic stress fields generates stress-induced elastic anisotropy. Here a rock specimen of Westerly granite was submitted to differential stress cycles (i.e., loading and unloading) of increasing amplitudes, up to failure and under upper crustal conditions. Combined records of strains, acoustic emissions, and *P* and *S* elastic wave anisotropies demonstrate that increasing differential stress promotes crack opening, sliding, and propagation subparallel to the main compressive stress orientation. However, the significant elastic anisotropies observed during loading (≥20%) almost vanish upon stress removal, demonstrating that in the absence of stress, crack-related elastic anisotropy remains limited (≤10%). As a consequence, (i) crack-related elastic anisotropies measured in the crust will likely be a strong function of the level of differential stress, and consequently (ii) continuous monitoring of elastic wave velocity anisotropy along faults could shed light on the mechanism of stress accumulation during interseismic loading.

Plain Language Summary In the upper crust, large strains are accommodated by brittle deformation mechanisms, leading to macroscopic faults embedded within a substantially damaged rock medium. The development of crack damage affects both the strength and the elastic and transport properties of rocks. Nowadays, the evolution of rock elastic properties is commonly used to estimate the direction of the maximum stress along faults and evaluate seismic hazard of seismogenic area. Up to now, stress-induced anisotropy was expected to be irreversible and observable by geophysics method even after unloading or exhumation of the rocks. In this study, we demonstrate for the first time that unloading induces an almost complete recovery of both stress-induced anisotropy and stress-induced damage. Our results suggest that elastic properties estimated from wave velocity measurement could then underestimate both damage and anisotropy of the crust under shallow depth conditions.

1. Introduction

In the upper crust, large strains are accommodated by brittle deformation mechanisms, leading to macroscopic faults embedded within a substantially damaged rock medium (Caine et al., 1996; Mitchell & Faulkner, 2008). Because the development of crack damage affects both the strength and the elastic and transport properties of rocks, characterizing the evolution of the physical properties of rocks has first-order implications on faulting and the mechanics of the upper crust. Nowadays, the evolution of rock elastic properties is commonly used to (i) estimate the direction of the maximum stress along faults (Boness & Zoback, 2004, 2006; M. L. Zoback & Zoback, 1980; M. D. Zoback & Zoback, 1991; M. D. Zoback et al., 1987), (ii) understand the fault and damage structure at depth (Hole et al., 1996), (iii) evaluate seismic hazard of seismogenic area (Quigley et al., 2012), and (iv) infer fluid overpressure in crustal fault zones (Kodaira et al., 2004).

Numerous experimental studies have been aimed at understanding brittle faulting in both crystalline and sedimentary rocks (Paterson & Wong, 2005). Before macroscopic failure, brittle rocks exhibit dilatancy (Brace & Byerlee, 1966) because of stable microcrack propagation. In crystalline rocks, microcrack propagation is dynamic enough to generate acoustic emissions (AEs) (Lockner et al., 1991; Scholz, 1968) and eventually

leads to strain localization (Hadley & Ward, 1975; Lockner et al., 1991). In porous rocks, however, microcracking can lead to cataclastic deformation associated with intense AEs activity (Fredrich et al., 1989; Menéndez et al., 1996; Wong & Baud, 2012; Wong et al., 1997), which can remain quasi-static and aseismic at the laboratory scale in some materials (Bonnelye et al., 2017a; Schubnel et al., 2007). Whether aseismic or seismic, distributed or localized, crack damage is nevertheless always accompanied by a decrease in both static (Blake & Faulkner, 2016; Brace & Bombolakis, 1963; Heap & Faulkner, 2008) and dynamic (i.e., ultrasonic wave velocities; Blake & Faulkner, 2016; Bonnelye et al., 2017b; Fortin et al., 2006, 2007; Nur & Simmons, 1969; Sarout & Guéguen, 2008a; Schubnel et al., 2003, 2006; Wang et al., 2013) elastic moduli. Furthermore, the propagation of preferentially oriented microcracks under stress also generates elastic anisotropy within the rock specimen (Johnson & Rasolofosaon, 1996; Nicolas et al., 2016; Sarout et al., 2014; Sayers & Kachanov, 1995; Schubnel & Guéguen, 2003; Wang et al., 2013). Until now, this crack-related stress-induced anisotropy was thought to remain permanently.

In a series of papers, which laid foundations to our theoretical understanding of the influence of crack damage on elastic rock deformation, Walsh(1965a, 1965b, 1965c) showed that cracks can indeed lead to a significant degradation of elastic properties and in fact control significantly the effective elastic properties of rocks. Theoretical studies (Guéguen & Sarout, 2011; Kachanov et al., 1994; Nishizawa, 1982) later extended this analysis to the case of anisotropic crack distribution and demonstrated that the development of anisotropic crack networks also leads to significant elastic anisotropy. On the other hand, microcrack propagation, dilatancy, and strength were successfully modeled using wing crack theory (Ashby & Sammis, 1990). However, although the wing crack theory predicts preferred orientations for crack propagation (Basista & Gross, 1998; Bhat et al., 2011; David et al., 2012), there is at present no unified micromechanical model which would predict the development of elastic anisotropy with wing crack propagation in rocks.

Finally, while most of the experimental and theoretical studies investigated the evolution of the elastic properties toward failure, little attention was given to their evolution during stress release. New insights could further our understanding of stress-induced anisotropy and healing processes, that is, the recovery of rock properties observed after earthquakes (Brenguier et al., 2008; Li et al., 2003, 2006; Schaff & Beroza, 2004). In order to address this issue, this article reports a detailed monitoring of the elastic properties of Westerly granite during a cyclic loading and unloading experiment up to failure, during which we monitor contemporaneously the evolution of strain, elastic wave anisotropy, and the development of damage. Using existing theories, we then investigate the micromechanics underlying stress-induced anisotropy and damage recovery in brittle rocks.

2. Methods

2.1. Experimental Apparatus

The apparatus used in this study is a triaxial oil medium loading cell built by Sanchez Technologies. The apparatus has been detailed, for example, in Passelègue et al. (2016). With this apparatus, confining pressure is applied on a rock cylinder (i.e., 80-mm length and 40-mm diameter) using two hydraulic servo pumps, applying radial and axial stress. The radial and axial stress can, respectively, go up to 100 and 680 MPa (for a sample of 40 mm diameter). The pressure transducers for both measurements have a resolution of 10^{-3} MPa. Three pairs of axial and radial 120 Ω quarter bridge strain gages were directly glued on the rock sample. Mechanical data were recorded at a frequency of 10 Hz during the entire experiment. Both increase and decrease of the stress are conducted at a constant stress rate (0.15 MPa/s), so that accurate stress and strain signals are recorded over the pressure ranges.

2.2. Acoustic Monitoring System

Twelve *P* sensors and four *S* sensors are used in this study. The sensors are used in two different ways: for velocity surveys, where each crystal is excited in turn and recordings are made on the others, and for AE monitoring in between each velocity survey. Pairs of *P* sensors were mounted facing each other in order to measure *P* wave velocities along several angles relative to the maximum compressive stress. *S* wave sensors were all mounted along the sample diameter, and the two pairs of *S* sensors were glued facing each other, in order to monitor shear wave velocities propagating in a horizontal direction but respectively polarized horizontally (S_h) and vertically (S_v). After the experiment, a reference survey (generally the one presenting the best wave arrivals) is chosen, and the flight times are picked manually. All other surveys are first picked automatically, using a conventional autopicking technique. The autopicking time only acts as a reference frame for subsequent cross-correlations over a 1-μs window with the reference survey. If the reference survey picking is robust, this combined approach minimizes the intrinsic errors of automatic picking process while enabling

cross correlations over small time windows relative to absolute variations in arrival times. Travel times are then estimated from the difference between *P* or *S* wave arrivals at each sensor location and the initiation time t_0 corresponding to the emission of the pulse by the source. Because the initiation time of the pulse and the locations of each sensor are well known, the measured travel time can be directly converted into a measure of the wave velocity along each raypath. Note that (i) lengths are not corrected for deformation, (ii) only raypaths going through the center of the specimen are considered, and (iii) measurements realized along the same angle relative to the maximum compressive stress are averaged.

AEs are also recorded continuously during our experiments. In this passive configuration, all sensors are used as receivers. The amplified signals are relayed to a trigger logic box and, if verifying a given pattern (i.e., a typical threshold amplitude of 150 mV for a minimum of three sensors with a 50-μs time window), are relayed and recorded by oscilloscopes at 10-MHz sampling frequency. This system allows recording up to 20 AEs/s. In the following, we will only show the cumulative count of AE data.

3. Experimental Results

3.1. Direct Measurements: Mechanical Data, Wave Velocities, and AEs

To study the development of anisotropy, a cyclic loading experiment was conducted on intact Westerly granite which presents a homogeneous grain size distribution and which is known to be an isotropic event at low pressure conditions (Scholz, 1986). The experiment was conducted at a constant confining pressure of 30 MPa under room humidity conditions. The summary of the experiment is detailed in Figure 1, reporting the evolution of (i) stresses (Figure 1a), (ii) axial (ε_1) and radial (ε_3) strains (Figure 1b), (iii) *P* and *S* wave velocities along different raypath angles (Figures 1c and 1d), and (iv) AEs (Figure 1e). During the increase of the confining pressure to 30 MPa, an increase in wave velocities is observed due to elastic crack closure Walsh (1965a), as observed in previous studies conducted on Westerly granite (Nasseri et al., 2009). The cyclic loading experiment consists of six different cycles, that is, increase of the axial stress to a target differential stress ($\sigma_D = \sigma_1 - \sigma_3$) and decrease back to hydrostatic stress conditions ($\sigma_1 = \sigma_3 = 30$ MPa). The target differential stress was increased for each subsequent cycle (Figure 1a), from $\sigma_D = 300$ MPa for the first cycle up to $\sigma_D = 469$ MPa for the last cycle during which macroscopic failure occurred.

During each cycle, increasing σ_D leads to an increase in the magnitude of the sample strains. While the evolution of the strain is almost linear during the initiation of loading, the trend departs from linearity when differential stress of each cycle is sufficiently high. This behavior is particularly clear from the radial strain measurement (Figure 1b) and is generally linked with the occurrence of AEs (Figure 1e). Below this threshold, the evolution of strain remains quasi-linear during the unloading part of each cycle, corresponding to the decrease of the differential stress back to hydrostatic conditions.

At the beginning of each cycle, a small change of both *P* and *S* wave velocities is observed. The maximum values are generally observed when $\sigma_D \approx 100$ MPa. Then, almost all wave velocities start to decrease with increasing σ_D. Using our sensor network, we monitor velocities following different raypath angles noted as C_n^{ϕ} in the following, where *n* is the nature of the elastic wave (compressional wave [*p*], preferentially vertical shear wave [*sv*], and preferentially horizontal shear wave [*sh*]), and ϕ is the angle with respect to σ_1. While all the raypaths tested are sensitive to loading, the radial raypath (C_p^{90} and C_{sh}) is the most affected as expected. The effect of loading on the acoustic velocities decreases with the angle of the raypath, and only slight decreases in velocity are observed for C_p^0 and C_{sv}^0 (Figures 1c and 1d). This decrease in wave velocity is well correlated with the evolution of the strain and the transition from elastic to inelastic behavior, marked by the yield point, that is, where the stress and strain relation departs from linearity. In addition, the stronger the acoustic activity, the more pronounced the decrease in wave velocities. Comparing each cycle with subsequent loading curves, we observed that no AEs occur within the specimen until the previous highest strain achieved during the previous cycle is exceeded. It also corresponds to the nonlinearity σ_D threshold, at about 90% of the previous maximum stress. This result has been recognized in previous studies (Browning et al., 2018; Holcomb, 1993; Kaiser, 1953; Lavrov, 2003; Lockner, 1993) and is known as the Kaiser effect.

During the unloading part of each cycle, a recovery in wave velocities is systematically observed. The amplitude of the recovery increases with decreasing σ_D. Only a fraction of the wave velocities is recovered during the first 100 MPa of the unloading (when $\sigma_D > 300$ MPa), highlighting a strong hysteresis. Then, the recovery evolves linearly with both strain and stress. The larger the differential stress achieved, the larger the decrease in wave velocities during loading and the larger the recovery during unloading (Figures 1c and 1d). However,

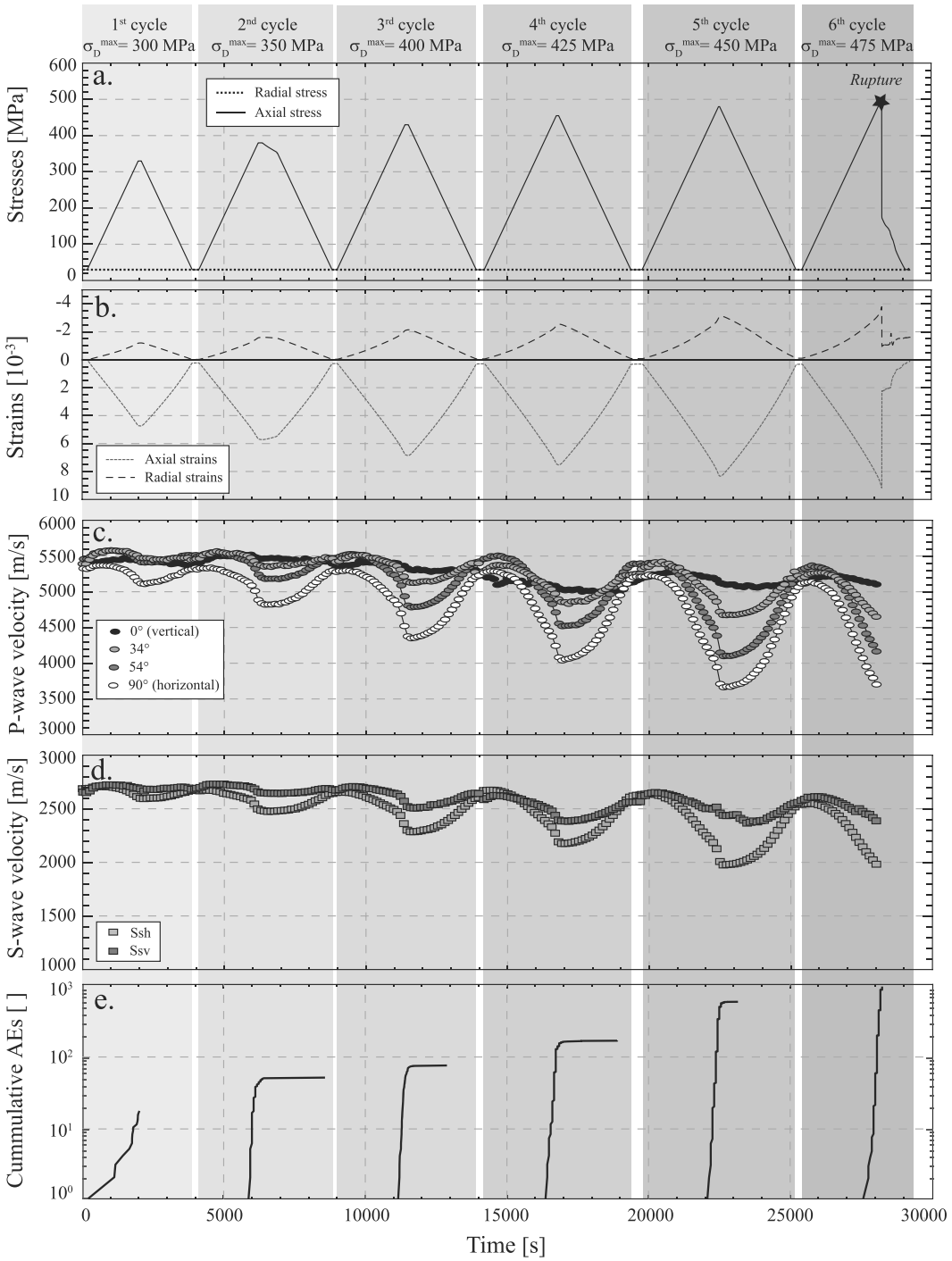

Figure 1. Overview of the experiment comprising six cycles. Evolution of (a) axial and radial stresses, (b) axial and radial strains, (c) *P* wave velocities in different directions, (d) horizontal and longitudinal *S* wave velocities, and (e) acoustic emissions activity during the experiment. The grayish colors, from light to darker as stress increases, are added to better highlight the six different cycles. The sample macroscopic failure during the sixth cycle is highlighted by a star on the stress curve. AE = acoustic emission.

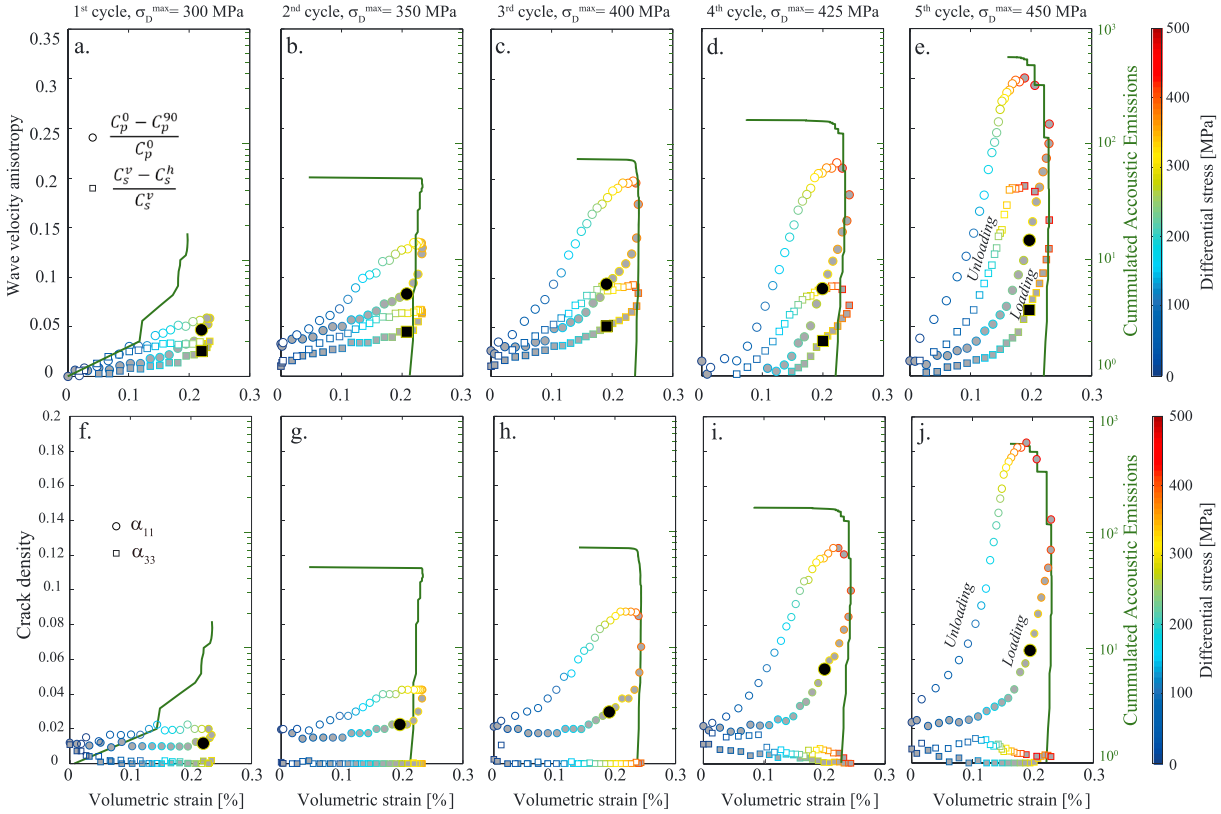

Figure 2. (a–e) Evolution of wave velocities anisotropy as a function of the volumetric strain during each cycle. Circles and squares correspond, respectively, to *P* and *S* wave velocity anisotropy. Gray symbols correspond to the loading stages and white symbols to the unloading stages. The color bar presents the evolution of the differential stress. The green line corresponds to the cumulative number of acoustic emissions recorded during each cycle. (f–j) Evolution of the crack density within the specimen as a function of the volumetric strain during each cycle. Circles and squares correspond, respectively, to the vertical (α_{11}) and the horizontal crack densities (α_{33}). Gray symbols correspond to the loading stages and white symbols to the unloading stages. The color bar presents the evolution of the differential stress. The green line corresponds to the cumulative number of acoustic emissions recorded during each cycle.

a small permanent decrease in wave velocities (about 1% of the initial wave velocity) is observed after each cycle (Figures 1c and 1d). This observation is in agreement with the finite strain recorded after each cycle, which increases also with the target differential stress achieved during loading (Figure 1b). This suggests that, although most damage has been recovered, small unrecoverable damage remains in the rock sample after each cycle.

3.2. Wave Anisotropy During Cycles

To investigate further the development of anisotropy during the experiment, we first present the evolution of two anisotropy parameters defined as $(C_p^0 - C_p^{90})/C_p^0$ and $(C_{sv} - C_{sh})/C_{sv}$ as a function of the volumetric strain and the differential stress during each cycle (Figures 2a–2e). While the rock is initially isotropic, both $(C_p^0 - C_p^{90})/C_p^0$ and $(C_{sv} - C_{sh})/C_{sv}$ increase with σ_D, and *P* wave velocity is particularly affected by anisotropy. During the first cycle ($\sigma_D^{max} = 300$ MPa), both $(C_p^0 - C_p^{90})/C_p^0$ and $(C_{sv} - C_{sh})/C_{sv}$ increase linearly with σ_D and the resulting volumetric strain. Only 16 AEs occurred during this cycle, suggesting that the sample remains almost purely elastic during the entire cycle. During the subsequent cycles, the same behavior is observed up to the initiation of acoustic activity when the yield point is reached, which enhances the rate of development of anisotropy (Figures 2b–2e). The maximum anisotropy in C_p and C_s increases with the target differential stress achieved. In addition, the value of anisotropy at a given differential stress increases for each subsequent loading. For instance, the value of $(C_p^0 - C_p^{90})/C_p^0$ at $\sigma_D = 270$ MPa is about 0.06 during the first cycle, 0.10 during the third cycle, and 0.13 during the fifth cycle (Figures 2a–2e).

During the unloading, the anisotropy for both C_p and C_s decreases to values close to the initial isotropic values. These results suggest that while loading induces anisotropic damage (highlighted by the occurrence of AEs) and crack opening in the rock sample (Figures 2a–2e), the anisotropy is almost entirely reversible, that is, the rock elastic isotropy is not affected by cumulative cycles. A strong hysteresis is observed between loading

and subsequent unloading stages. When unloading initiates, the wave anisotropy remains almost constant but then shows a strong decrease. It indicates that a nonnegligible release of stress is required to initiate anisotropy recovery. The magnitude of the stress release required to initiate recovery remains similar with increasing the target σ_D (Figures 2a–2e).

4. Inferring Crack Density and Orientation From Elastic Anisotropy

The *P* and *S* wave velocity measurements along different raypaths can be used to estimate the evolution of crack development during the experiment (Brantut et al., 2010; Fortin et al., 2011; Kovalyshen et al., 2016; Sarout & Guéguen, 2008a; Sayers & Kachanov, 1995). The transversely isotropic crack distribution is defined in the following by the vertical crack densities $\alpha_{11} = \alpha_{22}$ and by the horizontal crack density α_{33}. The method used to estimate α_{11} and α_{33} is detailed in Sarout and Guéguen (2008a) and Brantut et al. (2010). The method consists of the minimization of the difference between the theoretical and the experimental wave velocities using a least absolute method. At each pressure step of velocity surveys, the inversion automatically finds the best solution for the transversely isotropic stiffness tensors C_{ij} and yields the fitted crack density tensor.

Under hydrostatic pressure conditions ($\sigma_1 = \sigma_2 = \sigma_3 = 30$ MPa), α_{11} and α_{33} present similar values, suggesting that cracks are randomly oriented and that the rock specimen is isotropic (Figures 2f–2l). At an early loading stage, α_{33} decreases toward 0 and remains the same during further loading. This indicates that the horizontal cracks close at early loading stages and do not reopen under larger σ_D. Similarly, during most of the cycles, α_{11} first decreases and then increases linearly with increasing σ_D to reach a maximum value. As the cycle number (i.e., the target σ_D) increases, the maximum value of α_{11} increases, that is, from 0.005 at the peak stress of the first cycle (Figure 2f) up to 0.133 for the fifth cycle (Figure 2l). Note that the occurrence of AEs during cycle correlates with the rate of development of α_{11}. Finally, as observed with wave velocity anisotropy, the value of α_{11} at a given differential stress increases for each subsequent loading (black symbols in Figures 2f–2l). For instance, the value of α_{11} at $\sigma_D = 270$ MPa is about 0.015 during the first cycle, 0.03 during the third cycle, and 0.062 during the fifth cycle (Figures 2f–2l).

During the early stages (i.e., the first 50 MPa) of unloading of each cycle, α_{11} remains close to its peak value achieved during loading. As stated previously, the activation of recovery mechanisms requires the loading to drop below a critical stress. With further unloading, α_{11} decreases down to values slightly larger than the one observed at the onset of loading (Figures 2f–2fl). While a strong recovery is observed during the unloading stage of each cycle, a part of the stress-induced damages remains visible without differential stress acting on the sample. This result mirrors the finite strain achieved between each cycle and with the slight decrease in the wave velocities at the end of each cycle (Figure 1). Finally, upon return to hydrostatic conditions after each loading, the values of α_{11} and α_{33} differ, suggesting that anisotropy is not entirely recovered and that vertical cracks remain partially open after unloading, impacting elastic velocities (Figures 2f–2l).

5. Complete Velocity Field Anisotropy and Implications on Physical Properties

Using the optimal crack density tensor obtained for each survey assuming a transverse isotropic crack distribution, elastic wave speed can be calculated for all raypath angles ϕ between 0° and 90° following (Guéguen & Sarout, 2011)

$$C_p(\phi) = [(C_{11}\sin^2\phi + C_{33}\cos 2\phi + C_{44} + \sqrt{M})/(2\rho)]^{1/2}, \quad (1)$$

$$C_{sv}(\phi) = [(C_{11}\sin^2\phi + C_{33}\cos^2\phi + C_{44} - \sqrt{M})/(2\rho)]^{1/2}, \quad (2)$$

$$C_{sh}(\phi) = [(C_{66}\sin^2\phi + C_{44}\cos^2\phi)/\rho]^{1/2}, \quad (3)$$

where

$$M = ((C_{11} - C_{44})\sin^2\phi - (C_{33} - C_{44})\cos^2\phi)^2 + ((C_{13} + C_{44})\sin^2(2\phi))^2, \quad (4)$$

and ρ is the material density. Equations (1) to (4) are used to compute the complete wave velocity field during the experiments. The evolution of C_p and C_s over $\phi \in [0° : 90°]$ during the last cycle ($\sigma_D^{max} = 450$ MPa) is reported in Figures 3a and 3b, respectively, for loading and unloading. The modeled velocities resulting from the inversion are in good agreement with the direct measurements (colored circle in Figures 3a and 3b),

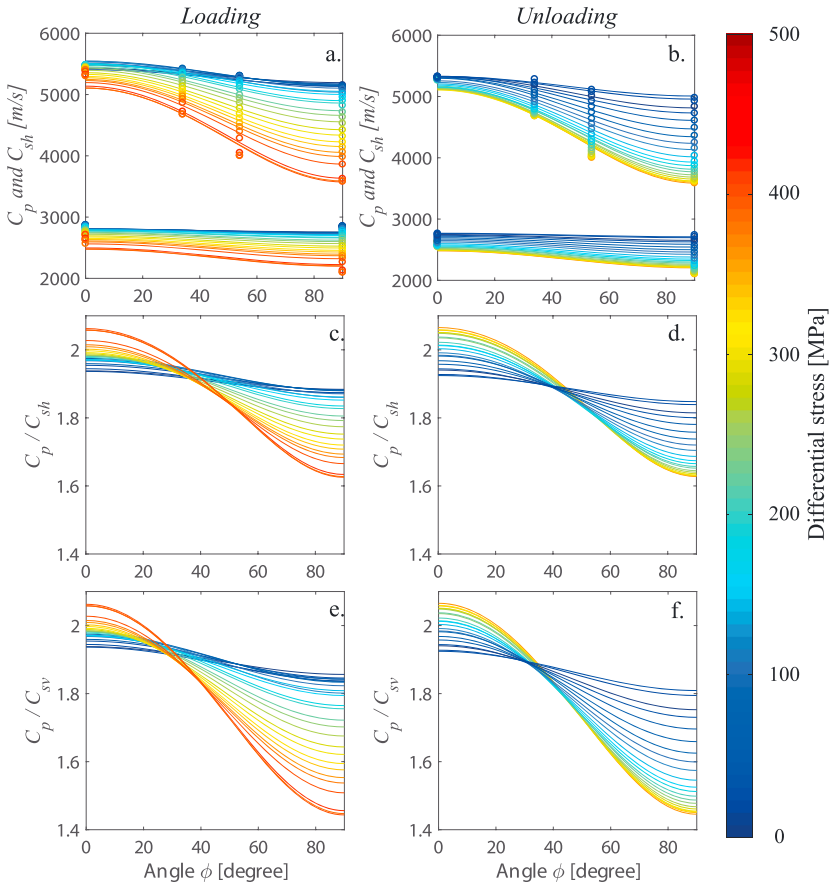

Figure 3. Evolution of the complete inverted velocity field and C_p/C_s ratios during the fifth cycle (target σ_D = 450 MPa). (a) and (b) compare the inverted velocities to the measured ones (colored circles) during, respectively, loading and unloading. (c) and (d) present the evolution of the inverted C_p/C_{sh} for all possible raypath angles during, respectively, loading and unloading. (e) and (f) present the evolution of the inverted C_p/C_{sv} for all possible raypath angles during, respectively, loading and unloading. In all plots, the color bar corresponds to the differential stress applied.

suggesting that all modeled values over $\phi \in [0° : 90°]$ provide good estimates. As observed from direct measurements (Figures 1c and 1d), increasing the angle of the raypath from 0° to 90° leads to a decrease in elastic wave velocities at a given differential stress (Figure 3a). Using the inverted velocity field allows the ratios C_p/C_{sh} and C_p/C_{sv}, commonly used in seismology, to be obtained as a function of the stress during the fifth cycle (Figures 3c and 3f). These ratios are a proxy for the effect of loading and unloading on the evolution of two of the three dynamic Poisson's ratios of the rock, assuming transverse isotropy. Interestingly, while both ratios C_p^0/C_s^0 (measured in the direction of σ_1) slightly increase from 1.95 to 2.05 with loading, C_p^{90}/C_s^{90} (measured in the direction of σ_3) strongly decrease from 1.85 to 1.6 for C_p^{90}/C_{sh}^{90} and from 1.85 to 1.42 for C_p^{90}/C_{sv}^{90} (Figure 3b). This result suggests that the development of stress-induced anisotropy affects the evolution of the Poisson's ratio, dependent on the stress orientation. The ratios C_p/C_s highly depend on (i) the raypath angle, that is, the orientation between the measurement and the principal stress, (ii) the amount of stress acting on the system, and (iii) the crack density and degree of initial damage, as observed in previous studies (Wang et al., 2012).

During unloading, both C_p and C_{sh} remain low during the first stage of the stress release ($\sigma_D > \approx$ 300 MPa; Figures 3b, 3d, and 3f). After this, reduction of the anisotropy occurs. C_p and C_s recover to values close to initial ones (Figure 3c), so that C_p^0/C_s^0 decreases back to 1.95 and C_p^{90}/C_s^{90} increases back to 1.85 (Figure 3d).

6. Interpretation and Discussion

In agreement with previous experimental (Bonnelye et al., 2017b; Schubnel & Guéguen, 2003; Stanchits et al., 2006; Thompson et al., 2006; Wang et al., 2012) and theoretical studies (Sarout & Guéguen, 2008b; Sayers & Kachanov, 1995), our experimental results demonstrate that anisotropy is induced as an intact rock is loaded

to macroscopic failure. During the first cycle ($\sigma_D^{max} = 300$ MPa), few AEs were recorded, and $C_p^0 \approx C_p^{90}$ and $C_{sh}^0 \approx C_{sh}^{90}$, suggesting that the rock deformed more or less isotropically. This further suggests that anisotropy starts to develop only beyond a critical state of stress. This critical level of stress could correspond to the stress required for (i) the onset of vertical cracks opening, (ii) the onset of slip along oblique cracks, or (iii) the onset of microcracking. Once anisotropy starts to develop, its evolution is affected by cumulative cycles (Figures 2a–2e). The larger the initial crack density within the rock specimen, the stronger the anisotropy at a given differential stress (Figure 2). Our results further suggest that, at least in dry conditions, the increase of anisotropy is both stress and damage dependent but that of the two, stress dependence of the anisotropy is by far the dominant factor. From the inverted crack density, the stress-induced anisotropy is explained by the development of vertical cracks during loading (Figures 2f–2l). Assuming that cracks are randomly oriented within the specimen when loading initiates, the opening of vertical cracks, by elastic loading of vertically oriented cracks or wing crack opening due to shear on oblique cracks, induces loss of contact along cracks which reduces the stiffness of the rock. Increasing the differential stress produces shear along cracks presenting a larger reactivation angle, explaining the nonlinear increase of α_{11} with σ_D. Note that our results were obtained during experiment conducted at room humidity conditions. In nature, rocks are expected to be saturated in fluid within the seismogenic crust, highlighted by both seismological (Audet et al., 2009; Kodaira et al., 2004) and field observations(Passelègue et al., 2014; Riedel et al., 2002; Rowe et al., 2009). Saturated condition is expected to reduce the anisotropy observed in *P* wave velocities due to the increase of the differential stress. However, the strong anisotropy observed in shear wave velocity is expected to remain observable. Our results are expected to remain observable in nature.

In contrast to previous experimental studies (Chen et al., 2011; Eslami et al., 2010; Heap & Faulkner, 2008; Heap et al., 2009; Kendrick et al., 2013; Pozdnyakova et al., 2009; Trippetta et al., 2013; Yang et al., 2015) which were mostly conducted under uniaxial conditions, our experimental results obtained under triaxial conditions show that subsequent unloading stage induces a strong recovery of both damage and anisotropy. While damage recovery was recently observed under isostatic stress conditions (Brantut, 2015) or during the cooling stage of thermal cycles (Griffiths et al., 2018), the recovery of anisotropy remained undocumented. Our results suggest that while cracks nucleate or propagate during loading (attested by the occurrence of AEs) increasing the crack lengths and the crack densities, unloading allows recovery of contact along cracks, due to elastic closure and back-sliding phenomena (Basista & Gross, 1998; David et al., 2012; Scholz & Kranz, 1974; Walsh & Brace, 1964) during unloading. The recovery of contact along cracks reduces the average crack lengths l_c which directly implies a strong decrease in crack densities ($\rho \propto \frac{\Sigma l_c^3}{V_{tot}}$), explaining the strong recovery in the elastic velocities. This effect of contact on crack densities, so called Island effect by Guéguen and Kachanov (2011), is expected to be a function of the location of the contact along the initial cracks. The maximum effect will be observed if contact is created in the central part of the initial cracks. However, while these contacts created during unloading are sufficient to increase the stiffness of the medium and recover the elastic properties of the rock, the propagation of the cracks during loading reduces the differential stress required to achieve the same strain compared to the precedent. The cumulative propagation of microcracks, that is, the increase of the crack density in the specimen, enhances stress-induced anisotropy during the subsequent loading (Figure 2).

The recovery observed during unloading stage of the experiment highlights that anisotropy and damage are highly stress dependent. Without differential stress, hydrostatic stress may be enough to close cracks, and hence, they are not observable from elastic properties. However, while a strong recovery is observed on wave velocity during subsequent unloading, damage produced during loading remains within the rock specimens and are expected to affect other physical properties, such as permeability or porosity (Sarout et al., 2017). Our results suggest that elastic measurement of natural rock samples should be made with both confining pressure and deviatoric stress to highlight the full amount of damage recorded from natural deformation under crustal pressure conditions. In addition, using the Kaiser effect, increasing the differential stress to the onset of AEs, that is, fast degradation of elastic waves, could allow estimation of the previous highest stress applied on the rocks in nature by tectonic loading.

These results suggest that the intensity of wave velocity anisotropy in the crust could be a proxy for the stress acting on the system. First, the orientation of the maximum stress acting on the fault is given by the direction of the fastest polarization, as previously observed in nature (Boness & Zoback, 2004, 2006; M. L. Zoback & Zoback, 1980; M. D. Zoback & Zoback, 1991; M. D. Zoback et al., 1987). Second, based on our experimental results, an increase of the stress in the crust is expected to lead to an increase of the anisotropy. This increase of

anisotropy is expected to be particularly strong and observable if (i) the system is close to the rupture point or (ii) if the medium is initially intensively damaged, as for example along fault at shallow depth (Hole et al., 1996; Mitchell & Faulkner, 2008). Monitoring continuous wave velocity anisotropy along faults could give important information about the evolution of stress in a fault system and could be used to image stress accumulation and stress rotation during interseismic loading. In addition, our results demonstrate that stress-induced anisotropy can lead to an increase of C_p/C_{sh} in the direction of the maximum stress when increasing the differential stress on the system and/or increasing the initial crack density. The increase in C_p^0/C_{sh}^0 recorded in this study leads to an increase in Poisson's ratio from 0.25 to 0.36 due to loading. These variations are in the range of the ones observed in subduction zones, where high pore fluid pressure has been inferred from geophysics measurement or field observations on fossil faults (Kodaira et al., 2004; Passelègue et al., 2014). Our results suggest that stress and anisotropic crack distribution could explain these observations, as suggested also in a previous study (Wang et al., 2012).

Acknowledgments
We thank A. Fagereng, M. Heap, and an anonymous reviewer for insightful reviews. We acknowledge the technical help of Yves Pinquier (ENS) during the course of the experiments. The data presented in this paper are available in the supporting information or by contacting the corresponding author at francois.passelegue@epfl.ch.

References

Ashby, M., & Sammis, C. (1990). The damage mechanics of brittle solids in compression. *Pure and Applied Geophysics*, *133*(3), 489–521.
Audet, P., Bostock, M. G., Christensen, N. I., & Peacock, S. M. (2009). Seismic evidence for overpressured subducted oceanic crust and megathrust fault sealing. *Nature*, *457*(7225), 76–78.
Basista, M., & Gross, D. (1998). The sliding crack model of brittle deformation: An internal variable approach. *International Journal of Solids and Structures*, *35*(5), 487–509.
Bhat, H., Sammis, C., & Rosakis, A. (2011). The micromechanics of Westerly granite at large compressive loads. *Pure and Applied Geophysics*, *168*(12), 2181–2198.
Blake, O., & Faulkner, D. (2016). The effect of fracture density and stress state on the static and dynamic bulk moduli of Westerly granite. *Journal of Geophysical Research: Solid Earth*, *121*, 2382–2399. https://doi.org/10.1002/2015JB012310
Boness, N. L., & Zoback, M. D. (2004). Stress-induced seismic velocity anisotropy and physical properties in the SAFOD Pilot Hole in Parkfield, CA. *Geophysical Research Letters*, *31*, L15S17. https://doi.org/10.1029/2003GL019020
Boness, N. L., & Zoback, M. D. (2006). Mapping stress and structurally controlled crustal shear velocity anisotropy in California. *Geology*, *34*(10), 825–828.
Bonnelye, A., Schubnel, A., David, C., Henry, P., Guglielmi, Y., Gout, C., et al. (2017a). Strength anisotropy of shales deformed under uppermost crustal conditions. *Journal of Geophysical Research: Solid Earth*, *122*, 110–129. https://doi.org/10.1002/2016JB013040
Bonnelye, A., Schubnel, A., David, C., Henry, P., Guglielmi, Y., Gout, C., et al. (2017b). Elastic wave velocity evolution of shales deformed under uppermost crustal conditions. *Journal of Geophysical Research: Solid Earth*, *122*(1), 130–141. https://doi.org/10.1002/2016JB013540
Brace, W. d., & Bombolakis, E. (1963). A note on brittle crack growth in compression. *Journal of Geophysical Research*, *68*(12), 3709–3713.
Brace, W. F., & Byerlee, J. D. (1966). Stick-slip as a mechanism for earthquakes. *Science*, *153*(3739), 990–992. https://doi.org/10.1126/science.153.3739.990
Brantut, N. (2015). Time-dependent recovery of microcrack damage and seismic wave speeds in deformed limestone. *Journal of Geophysical Research: Solid Earth*, *120*, 8088–8109. https://doi.org/10.1002/2015JB012324
Brantut, N., Schubnel, A., Corvisier, J., & Sarout, J. (2010). Thermochemical pressurization of faults during coseismic slip. *Journal of Geophysical Research*, *115*, B05314. https://doi.org/10.1029/2009JB006533
Brenguier, F., Campillo, M., Hadziioannou, C., Shapiro, N., Nadeau, R. M., & Larose, E. (2008). Postseismic relaxation along the San Andreas Fault at Parkfield from continuous seismological observations,. *Science*, *321*(5895), 1478–1481.
Browning, J., Meredith, P., Stuart, C., Harland, S., Healy, D., & Mitchell, T. (2018). A directional crack damage memory effect in sandstone under true triaxial loading. *Geophysical Research Letters*, *45*. https://doi.org/10.1029/2018GL078207
Caine, J. S., Evans, J. P., & Forster, C. B. (1996). Fault zone architecture and permeability structure. *Geology*, *24*(11), 1025–1028.
Chen, Y., Watanabe, K., Kusuda, H., Kusaka, E., & Mabuchi, M. (2011). Crack growth in Westerly granite during a cyclic loading test. *Engineering Geology*, *117*(3–4), 189–197. https://doi.org/10.1016/j.enggeo.2010.10.017
David, E., Brantut, N., Schubnel, A., & Zimmerman, R. W. (2012). Sliding crack model for nonlinearity and hysteresis in the uniaxial stress–strain curve of rock. *International Journal of Rock Mechanics and Mining Sciences*, *52*, 9–17.
Eslami, J., Grgic, D., & Hoxha, D. (2010). Estimation of the damage of a porous limestone from continuous (P- and S-) wave velocity measurements under uniaxial loading and different hydrous conditions. *Geophysical Journal International*, *183*(3), 1362–1375. https://doi.org/10.1111/j.1365-246X.2010.04801.x
Fortin, J., Guéguen, Y., & Schubnel, A. (2007). Effects of pore collapse and grain crushing on ultrasonic velocities and V_p/V_s. *Journal of Geophysical Research*, *112*, B08207. https://doi.org/10.1029/2005JB004005
Fortin, J., Stanchits, S., Dresen, G., & Guéguen, Y. (2006). Acoustic emission and velocities associated with the formation of compaction bands in sandstone. *Journal of Geophysical Research*, *111*, B10203. https://doi.org/10.1029/2005JB003854
Fortin, J., Stanchits, S., Vinciguerra, S., & Géguen, Y. (2011). Influence of thermal and mechanical cracks on permeability and elastic wave velocities in a basalt from Mt. Etna volcano subjected to elevated pressure. *Tectonophysics*, *503*(1–2), 60–74. https://doi.org/10.1016/j.tecto.2010.09.028, Thermo-Hydro-Chemo-Mechanical Couplings in Rock Physics and Rock Mechanics.
Fredrich, J. T., Evans, B., & Wong, T.-F. (1989). Micromechanics of the brittle to plastic transition in Carrara marble. *Journal of Geophysical Research*, *94*(B4), 4129–4145.
Griffiths, L., Lengliné, O., Heap, M., Baud, P., & Schmittbuhl, J. (2018). Thermal cracking in Westerly granite monitored using direct wave velocity, coda wave interferometry, and acoustic emissions. *Journal of Geophysical Research: Solid Earth*, *123*, 2246–2261. https://doi.org/10.1002/2017JB015191
Guéguen, Y., & Kachanov, M. (2011). Effective elastic properties of cracked rocks: An overview. In *Mechanics of crustal rocks* (pp. 73–125). Vienna: Springer.
Guéguen, Y., & Sarout, J. (2011). Characteristics of anisotropy and dispersion in cracked medium. *Tectonophysics*, *503*(1-2), 165–172.
Hadley, D., & Ward, I. (1975). Anisotropic and nonlinear viscoelastic behaviour in solid polymers. *Reports on Progress in Physics*, *38*(10), 1143.
Heap, M., & Faulkner, D. (2008). Quantifying the evolution of static elastic properties as crystalline rock approaches failure. *International Journal of Rock Mechanics and Mining Sciences*, *45*(4), 564–573.

Heap, M. J., Vinciguerra, S., & Meredith, P. (2009). The evolution of elastic moduli with increasing crack damage during cyclic stressing of a basalt from Mt. Etna volcano. *Tectonophysics*, *471*(1), 153–160.
Holcomb, D. J. (1993). General theory of the Kaiser effect, *International Journal of Rock Mechanics and Mining Sciences & Geomechanics Abstracts* (vol. 30, pp. 929–935). Madison, Wisconsin: Elsevier.
Hole, J. A., Thybo, H., & Klemperer, S. L. (1996). Seismic reflections from the near-vertical San Andreas Fault. *Geophysical Research Letters*, *23*(3), 237–240. https://doi.org/10.1029/96GL00019
Johnson, P. A., & Rasolofosaon, P. N. J. (1996). Nonlinear elasticity and stress-induced anisotropy in rock. *Journal of Geophysical Research*, *101*(B2), 3113–3124.
Kachanov, M., Tsukrov, I., & Shafiro, B. (1994). Effective moduli of solids with cavities of various shapes. *Applied Mechanics Reviews*, *47*(1), S151—S174.
Kaiser, J. (1953). *Erkenntnisse und Folgerungen aus der Messung von Geräuschen bei Zugbeanspruchung von metallischen Werkstoffen*. Archiv Eisenhuttenwesen: Verlag Stahleisen.
Kendrick, J. E., Smith, R., Sammonds, P., Meredith, P. G., Dainty, M., & Pallister, J. S. (2013). The influence of thermal and cyclic stressing on the strength of rocks from Mount St. Helens, Washington. *Bulletin of Volcanology*, *75*(7), 1–12. https://doi.org/10.1007/s00445-013-0728-z
Kodaira, S., Iidaka, T., Kato, A., Park, J.-O., Iwasaki, T., & Kaneda, Y. (2004). High pore fluid pressure may cause silent slip in the Nankai trough. *Science*, *304*(5675), 1295–1298.
Kovalyshen, Y., Sarout, J., & Dautriat, J. (2016). Inversion of ultrasonic data for transversely isotropic media. *Geophysics*, *82*(1), C1–C7.
Lavrov, A. (2003). The Kaiser effect in rocks: Principles and stress estimation techniques. *International Journal of Rock Mechanics and Mining Sciences*, *40*(2), 151–171.
Li, Y.-G., Chen, P., Cochran, E. S., Vidale, J. E., & Burdette, T. (2006). Seismic evidence for rock damage and healing on the San Andreas Fault associated with the 2004 M 6.0 Parkfield earthquake. *Bulletin of the Seismological Society of America*, *96*(4B), S349–S363.
Li, Y.-G., Vidale, J. E., Day, S. M., Oglesby, D. D., & Cochran, E. (2003). Postseismic fault healing on the rupture zone of the 1999 M 7.1 Hector Mine, California, earthquake. *Bulletin of the Seismological Society of America*, *93*(2), 854–869.
Lockner, D. (1993). The role of acoustic emission in the study of rock fracture. *International Journal of Rock Mechanics and Mining Sciences & Geomechanics Abstracts*, *30*(7), 883–899. https://doi.org/10.1016/0148-9062(93)90041-B
Lockner, D., Byerlee, J., Kuksenko, V., Ponomarev, A., & Sidorin, A. (1991). Quasi-static fault growth and shear fracture energy in granite. *Nature*, *350*(6313), 39–42.
Menéndez, B., Zhu, W., & Wong, T.-F. (1996). Micromechanics of brittle faulting and cataclastic flow in Berea sandstone. *Journal of Structural Geology*, *18*(1), 1–16.
Mitchell, T., & Faulkner, D. (2008). Experimental measurements of permeability evolution during triaxial compression of initially intact crystalline rocks and implications for fluid flow in fault zones. *Journal of Geophysical Research*, *113*, B11412. https://doi.org/10.1029/2008JB005588
Nasseri, M., Schubnel, A., Benson, P., & Young, R. (2009). Common evolution of mechanical and transport properties in thermally cracked Westerly granite at elevated hydrostatic pressure. *Pure and Applied Geophysics*, *166*(5-7), 927–948.
Nicolas, A., Fortin, J., Regnet, J., Dimanov, A., & Guéguen, Y. (2016). Brittle and semi-brittle behaviours of a carbonate rock: Influence of water and temperature. *Geophysical Journal International*, *206*(1), 438–456.
Nishizawa, O. (1982). Seismic velocity anisotropy in a medium containing oriented cracks. *Journal of Physics of the Earth*, *30*(4), 331–347.
Nur, A., & Simmons, G. (1969). Stress-induced velocity anisotropy in rock: An experimental study. *Journal of Geophysical Research*, *74*(27), 6667–6674.
Passelègue, F. X., Fabbri, O., Dubois, M., & Ventalon, S. (2014). Fluid overpressure along an Oligocene out-of-sequence thrust in the Shimanto Belt, SW Japan. *Journal of Asian Earth Sciences*, *86*, 12–24.
Passelègue, F., Schubnel, A., Nielsen, S., Bhat, H. S., Deldicque, D., Madariaga, R., et al. (2016). Dynamic rupture processes inferred from laboratory micro-earthquakes. *Journal of Geophysical Research: Solid Earth*, *121*, 4343–4365. https://doi.org/10.1002/2015JB012694
Paterson, M. S., & Wong, T.-f. (2005). *Experimental rock deformation—The Brittle Field*. Berlin, Heidelberg: Springer Science & Business Media.
Pozdnyakova, I., Bruno, G., Efremov, A. M., Clausen, B., & Hughes, D. (2009). Stress-dependent elastic properties of porous microcracked ceramics. *Advanced Engineering Materials*, *11*(12), 1023–1029. https://doi.org/10.1002/adem.200900192
Quigley, M., Van Dissen, R., Litchfield, N., Villamor, P., Duffy, B., Barrell, D., et al. (2012). Surface rupture during the 2010 M_w 7.1 Darfield (Canterbury) earthquake: Implications for fault rupture dynamics and seismic-hazard analysis. *Geology*, *40*(1), 55–58.
Riedel, M., Spence, G., Chapman, N., & Hyndman, R. (2002). Seismic investigations of a vent field associated with gas hydrates, offshore Vancouver Island. *Journal of Geophysical Research*, *107*(B9), 2200. https://doi.org/10.1029/2001JB000269
Rowe, C. D., Meneghini, F., & Moore, J. C. (2009). Fluid-rich damage zone of an ancient out-of-sequence thrust, Kodiak Islands, Alaska. *Tectonics*, *28*, TC1006. https://doi.org/10.1029/2007TC002126
Sarout, J., Cazes, E., Delle Piane, C., Arena, A., & Esteban, L. (2017). Stress-dependent permeability and wave dispersion in tight cracked rocks: Experimental validation of simple effective medium models. *Journal of Geophysical Research: Solid Earth*, *122*, 6180–6201. https://doi.org/10.1002/2017JB014147
Sarout, J., Esteban, L., Delle Piane, C., Maney, B., & Dewhurst, D. N. (2014). Elastic anisotropy of Opalinus Clay under variable saturation and triaxial stress. *Geophysical Journal International*, *198*(3), 1662–1682.
Sarout, J., & Guéguen, Y. (2008a). Anisotropy of elastic wave velocities in deformed shales: Part 1—Experimental results. *Geophysics*, *73*(5), D75–D89.
Sarout, J., & Guéguen, Y. (2008b). Anisotropy of elastic wave velocities in deformed shales: Part 2—Modeling results. *Geophysics*, *73*(5), D91—D103.
Sayers, C., & Kachanov, M. (1995). Microcrack-induced elastic wave anisotropy of brittle rocks. *Journal of Geophysical Research*, *100*(B3), 4149–4156.
Schaff, D. P., & Beroza, G. C. (2004). Coseismic and postseismic velocity changes measured by repeating earthquakes. *Journal of Geophysical Research*, *109*, B10302. https://doi.org/10.1029/2004JB003011
Scholz, C. (1968). Mechanism of creep in brittle rock. *Journal of Geophysical Research*, *73*(10), 3295–3302.
Scholz, C. H. (1986). Preface: A short geophysical history of Westerly granite. *Geophysical Monograph Series*, *37*, 9.
Scholz, C. H., & Kranz, R. (1974). Notes on dilatancy recovery. *Journal of Geophysical Research*, *79*(14), 2132–2135.
Schubnel, A., Benson, P. M., Thompson, B. D., Hazzard, J. F., & Young, R. P. (2006). Quantifying damage, saturation and anisotropy in cracked rocks by inverting elastic wave velocities. *Pure and Applied Geophysics*, *163*(5-6), 947–973.
Schubnel, A., & Guéguen, Y. (2003). Dispersion and anisotropy of elastic waves in cracked rocks. *Journal of Geophysical Research*, *108*(B2), 2101. https://doi.org/10.1029/2002JB001824

Schubnel, A., Nishizawa, O., Masuda, K., Lei, X., Xue, Z., & Guéguen, Y. (2003). Velocity measurements and crack density determination during wet triaxial experiments on Oshima and Toki granites. *Thermo-Hydro-Mechanical Coupling in Fractured Rock*, *160*, 869–887.

Schubnel, A., Thompson, B., Fortin, J., Guéguen, Y., & Young, R. (2007). Fluid-induced rupture experiment on Fontainebleau sandstone: Premonitory activity, rupture propagation, and aftershocks. *Geophysical Research Letters*, *34*, L19307. https://doi.org/10.1029/2007GL031076

Stanchits, S., Vinciguerra, S., & Dresen, G. (2006). Ultrasonic velocities, acoustic emission characteristics and crack damage of basalt and granite. *Pure and Applied Geophysics*, *163*(5-6), 975–994.

Thompson, B. D., Young, R. P., & Lockner, D. A. (2006). Fracture in Westerly granite under AE feedback and constant strain rate loading: Nucleation, quasi-static propagation, and the transition to unstable fracture propagation, *Rock damage and fluid transport, part I* (pp. 995–1019). Basel: Springer.

Trippetta, F., Collettini, C., Meredith, P., & Vinciguerra, S. (2013). Evolution of the elastic moduli of seismogenic triassic evaporites subjected to cyclic stressing. *Tectonophysics*, *592*, 67–79. https://doi.org/10.1016/j.tecto.2013.02.011

Walsh, J. (1965a). The effect of cracks on the uniaxial elastic compression of rocks. *Journal of Geophysical Research*, *70*(2), 399–411.

Walsh, J. (1965b). The effect of cracks on the compressibility of rock. *Journal of Geophysical Research*, *70*(2), 381–389.

Walsh, J. (1965c). The effect of cracks in rocks on Poisson's ratio. *Journal of Geophysical Research*, *70*(20), 5249–5257.

Walsh, J. B., & Brace, W. (1964). A fracture criterion for brittle anisotropic rock. *Journal of Geophysical Research*, *69*(16), 3449–3456.

Wang, X.-Q., Schubnel, A., Fortin, J., David, E. C., Guéguen, Y., & Ge, H.-K. (2012). High Vp/Vs ratio: Saturated cracks or anisotropy effects?*Geophysical Research Letters*, *39*, l11307. https://doi.org/10.1029/2012GL051742

Wang, X.-Q., Schubnel, A., Fortin, J., Guéguen, Y., & Ge, H.-K. (2013). Physical properties and brittle strength of thermally cracked granite under confinement. *Journal of Geophysical Research: Solid Earth*, *118*, 6099–6112. https://doi.org/10.1002/2013JB010340

Wong, T.-f., & Baud, P. (2012). The brittle-ductile transition in porous rock: A review. *Journal of Structural Geology*, *44*, 25–53.

Wong, T.-f., David, C., & Zhu, W. (1997). The transition from brittle faulting to cataclastic flow in porous sandstones: Mechanical deformation. *Journal of Geophysical Research*, *102*(B2), 3009–3025.

Yang, S.-Q., Ranjith, P. G., Huang, Y.-H., Yin, P.-F., Jing, H.-W., Gui, Y.-L., & Yu, Q.-L. (2015). Experimental investigation on mechanical damage characteristics of sandstone under triaxial cyclic loading. *Geophysical Journal International*, *201*(2), 662–682. https://doi.org/10.1093/gji/ggv023

Zoback, M. L., & Zoback, M. (1980). State of stress in the conterminous United States. *Journal of Geophysical Research: Solid Earth*, *85*(B11), 6113–6156.

Zoback, M. D., & Zoback, M. L. (1991). Tectonic stress field of North America and relative plate motions. *Neotectonics of North America*, *1*, 339–366.

Zoback, M. D., Zoback, M. L., Mount, V. S., Suppe, J., Eaton, J. P., Healy, J. H., et al. (1987). New evidence on the state of stress of the San Andreas Fault System. *Science*, *238*(4830), 1105–1111.